European Journal of Mechanics / B Fluids 102 (2023) 18–30

Contents lists available at ScienceDirect

European Journal of Mechanics / B Fluids

journal homepage: www.elsevier.com/locate/ejmflu

A new IBL model for quasi-unidirectional gravity-driven flow over topography

S.J.D. D'Alessio

Faculty of Mathematics, University of Waterloo, Waterloo, Ontario, N2L 3G1, Canada

ARTICLE INFO

Article history:
Received 23 March 2023
Received in revised form 5 July 2023
Accepted 11 July 2023
Available online 17 July 2023

Keywords:
Steady
Unsteady
Viscous
Three dimensional
Integral boundary layer
Gravity driven

ABSTRACT

Discussed in this investigation is the three-dimensional gravity-driven flow of a thin fluid layer down an incline and over topography. A new three-dimensional integral-boundary-layer (IBL) model is proposed to describe the flow. Numerical simulations are presented and comparisons with lubrication and two-dimensional IBL models are discussed for both steady and unsteady flows. Subcritical and supercritical cases are considered, along with symmetrical and asymmetrical bottom topographies. Also, good agreement was found with experiments.

1. Introduction

Falling thin fluid layers occur often in a variety of settings [1–3]. For example, in industrial applications such layers can act as a coat to protect a surface as in bearings, painting and other manufacturing processes [4]. In the environment thin flows can be found in rivers or may appear as lava flows [5,6], ice flows [7], mud slides [8] or even avalanches [9]. In living organisms thin fluid layers can play important roles such as lining the airways in the lungs or forming a protective surface on the front of the eye as in the case of a tear film [10]. Other examples include thin flows in human-made structures such as aqueducts and spillways. Since thin fluid layers are prone to interfacial instabilities, variations in fluid thickness can occur which can lead to the formation of relatively large amplitude waves along the surface. In some situations such waves can have an adverse effect, as in coating applications where they can produce an uneven coating. Because of this, thin fluid layers have been studied extensively on various levels: experimentally, theoretically, and numerically [11–17]. In many previous investigations such flows were approximated as two dimensional, whereas in this study we investigate three-dimensional flows over various two-dimensional topographies which are much more realistic. Also, the proposed model applies to an arbitrary bottom topography.

Considerable effort has been invested in modelling thin fluid layers. One class of models is known as integral-boundary-layer (IBL) models [15]. The basic idea behind these models is first to simplify the governing Navier–Stokes equations by formulating them in terms of a shallowness parameter and neglecting terms that are deemed to be small. Next, the cross-stream dependence is eliminated by depth-integrating the equations and prescribing the velocity variation with respect to depth. Another class of models is known as weighted-residual models (WRM) originally proposed by Ruyer-Quil and Manneville [16,17] to handle isothermal flows down an even incline. Since then it has been applied to more complicated flows. For example, Kalliadasis et al. [18] extended the weighted-residual method to model flows down an even heated incline, D'Alessio et al. [19] used it to model isothermal flows over a wavy incline, while D'Alessio and Pascal [20] successfully applied it to inclined isothermal flows down an uneven porous surface. Several other extensions such as incorporating surfactants [21] and heated flows over wavy surfaces [22,23] have also been advanced. Although most of the above cited WRM developed are second order, Veremieiev and Wacks [24] have extended the weighted-residual method to include third and fourth-order terms. Slow viscous motion of a thin fluid layer can also be modelled using lubrication theory, or as Stokes flow [25–33], and many of these investigations are summarized in the review by Aksel and Schörner [34].

The work in modelling three-dimensional thin fluid layers is relatively rare compared to two-dimensional fluid layers. Here, we will focus on some previous studies pertaining to three-dimensional flows spreading over topography. Baxter et al. [29] considered steady gravity-driven Stokes flow down an incline and over hemispherical obstacles. The controlling parameters in their investigation were the angle of inclination, the Bond number, and the obstacle geometry. A key finding is that the free

E-mail address: sdalessio@uwaterloo.ca.

https://doi.org/10.1016/j.euromechflu.2023.07.004
0997-7546/

surface profiles had a peak upstream of the obstacle followed by a downstream trough. They also considered cases where the obstacle penetrates the free surface, and in such cases a contact angle was specified. The study by Buttle et al. [35], on the other hand, considered the steady flow of an ideal fluid using a boundary-integral method. Both subcritical and supercritical regimes were explored for a variety of bottom configurations. Their focus was on the nonlinear features of the wave patterns and their relationship to ship wakes. Veremieiev et al. [36,37] numerically investigated two and three-dimensional flow over step-like and trench topographies and obtained good agreement with the experimental results of Decré and Baret [38]. Three-dimensional flows over a wavy bottom was studied theoretically by Trifonov [39]; he derived a thin-film IBL model. Heining et al. [40] also worked on three-dimensional flows over a wavy bottom and solved the problem analytically, numerically and experimentally. Lastly, Hinton et al. [30] investigated the flow of a viscous free surface over bottom topography theoretically and numerically through the lens of lubrication theory. Their work was motivated by the interaction of lava flows with obstructions. They considered cases where the topography penetrated the free surface, which they termed dry zones, and where dry zones would form in the wake of an obstacle. Rather than specifying a contact angle, they handled dry zones by introducing a small source term which had the effect of creating a virtual thin film over the dry zone.

In the present work we also investigate three-dimensional gravity-driven flow over topography. However, the approach is different from the previous studies discussed in several respects. First, we consider both steady and unsteady flows and we are only concerned with dry-free zones (i.e. fully submerged topographies). In addition, several bottom topographies are entertained including smooth localized bumps, wavy periodic undulations, and a steep-sided trench. Second, a new IBL model to describe the flow is proposed. This model takes into account both viscous and inertial effects, and hence, is inherently nonlinear. It can be thought of as a hybrid model bridging lubrication theory and integral-boundary-layer formalism. This approach is novel in the sense that to our knowledge it has never been attempted. We conduct numerous numerical experiments of subcritical and supercritical flows, outline some differences between two and three-dimensional flows, and make comparisons with a lubrication model to illustrate some deficiencies in lubrication theory. Third, the proposed model is validated by drawing comparisons with the experiments conducted in [40] for the case of a two-dimensional wavy topography. The above factors distinguishes this study from the previous ones listed. The paper is structured as follows. In the next section we formulate the problem and derive the IBL model. Following that, in Section 3 a numerical solution procedure is proposed to solve the model equations. Numerical results using Neumann and periodic boundary conditions are then presented and discussed in Section 4 for various topographies. Comparisons are made with a three-dimensional steady lubrication model, an unsteady two-dimensional IBL model, and experiments. Finally, in Section 5 we summarize the key findings.

2. Mathematical formulation

We consider the three-dimensional, laminar, gravity-driven isothermal flow of a viscous, incompressible, Newtonian, shallow liquid layer of thickness $h(x, y, t)$ down a non-porous surface which is inclined at an angle of β with the horizontal. The surface over which the fluid is flowing has a variable bottom topography denoted by $\mathcal{M}m(x, y)$. We define a coordinate system (x, y, z) such that the down-slope coordinate is x, the cross-slope coordinate is y, and the normal coordinate above the inclined surface is z. Illustrated in Fig. 1 is a cross-sectional view in the x direction taken along the line of symmetry for the case of symmetric bottom topography.

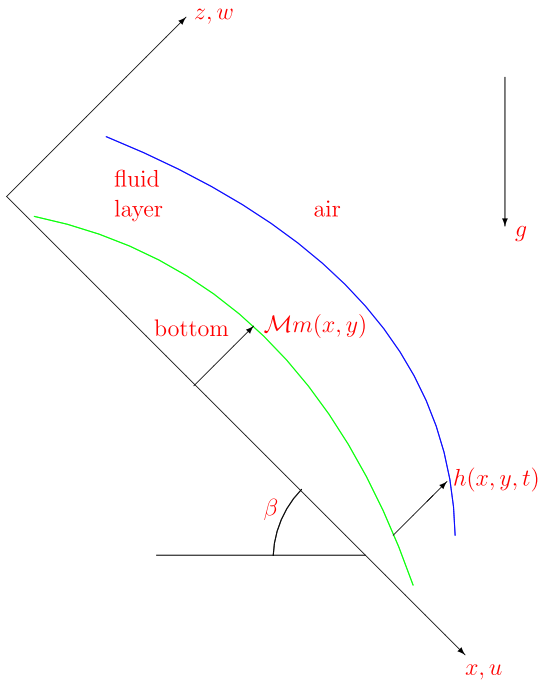

Fig. 1. Cross section of the flow and setup.

The continuity and Navier–Stokes equations expressed in dimensional form are given by

$$\frac{\partial u}{\partial x}+\frac{\partial v}{\partial y}+\frac{\partial w}{\partial z}=0\,,$$

$$\rho\left(\frac{\partial u}{\partial t}+u\frac{\partial u}{\partial x}+v\frac{\partial u}{\partial y}+w\frac{\partial u}{\partial z}\right)=-\frac{\partial p}{\partial x}+\rho g\sin\beta + \mu\left(\frac{\partial^2 u}{\partial x^2}+\frac{\partial^2 u}{\partial y^2}+\frac{\partial^2 u}{\partial z^2}\right)\,,$$

$$\rho\left(\frac{\partial v}{\partial t}+u\frac{\partial v}{\partial x}+v\frac{\partial v}{\partial y}+w\frac{\partial v}{\partial z}\right) =-\frac{\partial p}{\partial y}+\mu\left(\frac{\partial^2 v}{\partial x^2}+\frac{\partial^2 v}{\partial y^2}+\frac{\partial^2 v}{\partial z^2}\right)\,,$$

$$\rho\left(\frac{\partial w}{\partial t}+u\frac{\partial w}{\partial x}+v\frac{\partial w}{\partial y}+w\frac{\partial w}{\partial z}\right)=-\frac{\partial p}{\partial z}-\rho g\cos\beta + \mu\left(\frac{\partial^2 w}{\partial x^2}+\frac{\partial^2 w}{\partial y^2}+\frac{\partial^2 w}{\partial z^2}\right)\,,$$

where u, v, w are the velocity components in the x, y, z directions, respectively, p is the pressure, g is the acceleration due to gravity, ρ is the density, and μ is the dynamic viscosity. We next cast the governing equations in dimensionless form. In order to achieve this we choose the Nusselt thickness of the liquid given by

$$H=\left(\frac{3\mu Q}{g\rho\sin\beta}\right)^{1/3}\,,$$

as the vertical length scale, while L to be the horizontal length scale. In the above Q denotes the prescribed flow rate per unit width. The velocity scale is taken to be $U = Q/H$ and the time

scale is L/U. For the pressure we use ρU^2 as the scale. Using these scales we apply the following transformation

$$(x, y, z) = (Lx^*, Ly^*, \text{Hz}^*)\ ,\ h = Hh^*\ , t = \frac{L}{U}t^*,$$
$$(u, v, w) = U(u^*, v^*, \frac{H}{L}w^*)\ ,\ p = \rho U^2 p^*\ .$$

With these scalings in place, and dropping the asterisks for notational convenience, the dimensionless equations within the liquid layer to second order in the shallowness parameter $\delta = H/L$ become

$$\frac{\partial u}{\partial x} + \frac{\partial v}{\partial y} + \frac{\partial w}{\partial z} = 0\ , \tag{1}$$

$$\delta Re\left(\frac{\partial u}{\partial t} + u\frac{\partial u}{\partial x} + v\frac{\partial u}{\partial y} + w\frac{\partial u}{\partial z}\right) = -\delta Re\frac{\partial p}{\partial x} + 3 + \delta^2\left(\frac{\partial^2 u}{\partial x^2} + \frac{\partial^2 u}{\partial y^2}\right) + \frac{\partial^2 u}{\partial z^2}\ , \tag{2}$$

$$\delta Re\left(\frac{\partial v}{\partial t} + u\frac{\partial v}{\partial x} + v\frac{\partial v}{\partial y} + w\frac{\partial v}{\partial z}\right) = -\delta Re\frac{\partial p}{\partial y} + \delta^2\left(\frac{\partial^2 v}{\partial x^2} + \frac{\partial^2 v}{\partial y^2}\right) + \frac{\partial^2 v}{\partial z^2}\ , \tag{3}$$

$$\delta^2 Re\left(\frac{\partial w}{\partial t} + u\frac{\partial w}{\partial x} + v\frac{\partial w}{\partial y} + w\frac{\partial w}{\partial z}\right) = -Re\frac{\partial p}{\partial z} - 3\cot\beta + \delta\frac{\partial^2 w}{\partial z^2}. \tag{4}$$

In the above $Re = \rho Q/\mu$ is the Reynolds number. These can be viewed as the long-wave equations and mark the starting point of our mathematical formulation.

Integrating Eq. (2) across the fluid layer from $z = \mathcal{M}m$ to $z = \mathcal{M}m + h$ and introducing the down-slope flow rate $q(x, y, t)$ defined by

$$q = \int_{\mathcal{M}m}^{\mathcal{M}m+h} u dz\ ,$$

leads to the following

$$\delta Re\left(\frac{\partial q}{\partial t} + \frac{\partial}{\partial x}\int_{\mathcal{M}m}^{\mathcal{M}m+h} u^2 dz + \frac{\partial}{\partial y}\int_{\mathcal{M}m}^{\mathcal{M}m+h} uv dz\right) = -\delta Re\int_{\mathcal{M}m}^{\mathcal{M}m+h}\frac{\partial p}{\partial x}dz + 3h + \delta^2\int_{\mathcal{M}m}^{\mathcal{M}m+h}\left(\frac{\partial^2 u}{\partial x^2} + \frac{\partial^2 u}{\partial y^2}\right)dz - \left.\frac{\partial u}{\partial z}\right|_{\mathcal{M}m}. \tag{5}$$

In arriving at this expression we made use of the kinematic condition

$$w = \frac{\partial h}{\partial t} + u\left(\frac{\partial h}{\partial x} + \mathcal{M}\frac{\partial m}{\partial x}\right) + v\left(\frac{\partial h}{\partial y} + \mathcal{M}\frac{\partial m}{\partial y}\right) \quad \text{on}\ \ z = \mathcal{M}m + h\ ,$$

as well as the zero-shear condition

$$\frac{\partial u}{\partial z} = 0\ \ \text{on}\ \ z = \mathcal{M}m + h\ .$$

In order to estimate the various integrals and the last term appearing on the right-hand side of Eq. (5), we need to specify u, v and p. For the velocity u we propose the following

$$u = \frac{3q}{2h^3}\left(2(\mathcal{M}m + h)z - z^2 - \mathcal{M}^2m^2 - 2\mathcal{M}hm\right)\ , \tag{6}$$

which satisfies the down-slope flow rate definition. This parabolic profile is the three-dimensional equivalent of that which is commonly used in modelling two-dimensional flows (for example, see [15–23]) and results from Eq. (2) by retaining only the dominant terms

$$\frac{\partial^2 u}{\partial z^2} + 3 = 0\ ,$$

and applying the no-slip condition $u = 0$ on $z = \mathcal{M}m$ and the above zero-shear condition. The profiles for v and p can be obtained by considering the following first-order equations based on (3) and (4)

$$\frac{\partial^2 v}{\partial z^2} = \delta Re\frac{\partial p}{\partial y}\ , \tag{7}$$

$$Re\frac{\partial p}{\partial z} = -3\cot\beta + \delta\frac{\partial^2 w}{\partial z^2}. \tag{8}$$

Since the pressure term in Eq. (5) is already multiplied by δ we only need to consider the first-order equation given by (8) to guarantee second-order accuracy. On the other hand, we retain first-order accuracy in the transverse component of velocity because we are dealing with flows that are mainly two-dimensional and in the down-slope direction with weak flow in the cross-slope direction.

Integrating (8) and applying the stress condition which to first order in δ is given by

$$p = \frac{2\delta}{Re}\frac{\partial w}{\partial z} \quad \text{on}\ \ z = \mathcal{M}m + h\ ,$$

leads to the following expression for the pressure

$$p = \frac{3\cot\beta}{Re}(\mathcal{M}m + h - z) + \frac{\delta}{Re}\frac{\partial w}{\partial z} + \left.\frac{\delta}{Re}\frac{\partial w}{\partial z}\right|_{\mathcal{M}m+h}\ , \tag{9}$$

where

$$\frac{\partial w}{\partial z} = -\left(\frac{\partial u}{\partial x} + \frac{\partial v}{\partial y}\right)\ .$$

Here, we have assumed that the Reynolds (Re) and Weber (We) numbers are of order unity, and thus, the effects of surface tension do not make an appearance. Now, substituting (9) into (7), integrating and applying the no-slip and zero-shear conditions

$$v = 0\ \ \text{on}\ z = \mathcal{M}m\ ,\ \frac{\partial v}{\partial z} = 0\ \ \text{on}\ \ z = \mathcal{M}m + h\ ,$$

yields

$$v = 3\delta\cot\beta\left(\frac{\partial h}{\partial y} + \mathcal{M}\frac{\partial m}{\partial y}\right)\left[\frac{1}{2}\left(z^2 - \mathcal{M}^2m^2\right) - (\mathcal{M}m + h)(z - \mathcal{M}m)\right]. \tag{10}$$

This equation for the transverse, or spanwise, velocity v is the same expression that emerges from lubrication theory (for example, see [30–33]), and it is proposed here as a means of extending flows that are predominantly two dimensional to three dimensions. Inserting (6), (9) and (10) into (5) one obtains the following evolution equation for the flow rate q after some algebra

$$\frac{\partial q}{\partial t} + \frac{\partial}{\partial x}\left(\frac{6}{5}\frac{q^2}{h} + \frac{3\cot\beta}{2Re}h^2\right) = \frac{3}{\delta Re}\left(h - \frac{q}{h^2}\right) - \frac{3\mathcal{M}\cot\beta}{Re}h\frac{\partial m}{\partial x} + \frac{\delta}{Re}\left[\frac{7}{2}\frac{\partial^2 q}{\partial x^2} - \frac{9q}{2h}\frac{\partial^2 h}{\partial x^2} - \frac{3\mathcal{M}q}{h}\frac{\partial^2 m}{\partial x^2} + \frac{6}{h}\left(\mathcal{M}\frac{\partial m}{\partial x} + \frac{3}{2}\frac{\partial h}{\partial x}\right)\times\left(\frac{q}{h}\frac{\partial h}{\partial x} - \frac{\partial q}{\partial x}\right) - \frac{6\mathcal{M}^2 q}{h^2}\left(\frac{\partial m}{\partial x}\right)^2 + \frac{\partial^2 q}{\partial y^2} - \frac{3q}{2h}\left(\frac{\partial^2 h}{\partial y^2} + \mathcal{M}\frac{\partial^2 m}{\partial y^2}\right)\right.$$

$$-\frac{3\mathcal{M}^2 q}{h^2}\left(\frac{\partial m}{\partial y}\right)^2 + \left(\frac{\partial h}{\partial y}+\mathcal{M}\frac{\partial m}{\partial y}\right)\left(\frac{3q}{h^2}\frac{\partial h}{\partial y}-\frac{3}{h}\frac{\partial q}{\partial y}\right)\Bigg] + \frac{6}{5}\delta\cot\beta h\left[\left(\mathcal{M}\frac{\partial m}{\partial y}+\frac{\partial h}{\partial y}\right)\left(h\frac{\partial q}{\partial y}+2q\frac{\partial h}{\partial y}\right) + hq\left(\frac{\partial^2 h}{\partial y^2}+\mathcal{M}\frac{\partial^2 m}{\partial y^2}\right)\right] . \tag{11}$$

An evolution equation for h can similarly be derived by considering the continuity Eq. (1). Integrating (1) across the fluid layer from $z = \mathcal{M}m$ to $z = \mathcal{M}m + h$ and implementing the kinematic condition along the free surface, the no-slip condition $w = 0$ at $z = \mathcal{M}m$, and Eq. (10) for v yields

$$\frac{\partial h}{\partial t}+\frac{\partial q}{\partial x} = \delta\cot\beta\frac{\partial}{\partial y}\left[h^3\left(\frac{\partial h}{\partial y}+\mathcal{M}\frac{\partial m}{\partial y}\right)\right] . \tag{12}$$

The nonlinear coupled system of Eqs. (11)–(12) together with initial conditions and appropriate conditions along the boundaries forms our three-dimensional (3D) IBL model for a specified bottom topography $\mathcal{M}m(x, y)$. Although most of the terms retained in these equations are correct to second order, the expression for v used in the derivation of (12) is first order; also, the shear conditions along the free surface correct to second order in δ are given by

$$\frac{\partial u}{\partial z} = \delta^2\left[2\frac{\partial \xi}{\partial x}\left(2\frac{\partial u}{\partial x}+\frac{\partial v}{\partial y}\right)+\frac{\partial \xi}{\partial y}\left(\frac{\partial u}{\partial y}+\frac{\partial v}{\partial x}\right)-\frac{\partial w}{\partial x}\right] ,$$

$$\frac{\partial v}{\partial z} = \delta^2\left[2\frac{\partial \xi}{\partial y}\left(2\frac{\partial v}{\partial y}+\frac{\partial u}{\partial x}\right)+\frac{\partial \xi}{\partial x}\left(\frac{\partial u}{\partial y}+\frac{\partial v}{\partial x}\right)-\frac{\partial w}{\partial y}\right] ,$$

where $\xi = h + \mathcal{M}m$ denotes the free surface. These have been simplified to the zero-shear conditions

$$\frac{\partial u}{\partial z} = \frac{\partial v}{\partial z} = 0 ,$$

and justification of this will be presented later. Thus, we think of the system (11)–(12) as a 1.5 order model. Lastly, we note that system (11)–(12) is invariant under the transformation

$$y \to -y , \quad v \to -v ,$$

since gravity acts in the $x - z$ plane. This symmetry property will be exploited when prescribing suitable cross-slope boundary conditions. This property was also reported in [40].

3. Numerical solution procedure

Eqs. (11)–(12) were solved on the rectangular domain $L_u \le x \le L_d$, $-W \le y \le W$ having a width $2W$ and a length $L_d - L_u$. Simulations were carried out using two types of boundary conditions along the boundaries. These include Neumann and periodic boundary conditions. The computational domain was discretized into I equally spaced subintervals in the x direction and J equally spaced subintervals in the y direction forming a network of $(I-1)\times(J-1)$ interior grid points (x_i, y_j) where $x_i = L_u + i\Delta x$, $i = 1, 2, \ldots, I-1$ and $y_j = -W + j\Delta y$, $j = 1, 2, \ldots, J-1$ with $\Delta x = (L_d - L_u)/I$ and $\Delta y = 2W/J$ denoting the uniform grid spacing in the x, y directions, respectively.

System (11)–(12) was solved using finite differences [41]. We begin by casting equations (11)–(12) in the generic form

$$\frac{\partial \chi}{\partial t} = R(x, y, t) , \tag{13}$$

where χ denotes either h or q, and the function $R(x, y, t)$ refers to all the remaining terms when brought to the right-hand side. Assuming the solution at time t is known, we can advance the solution to time $t + \Delta t$ by integrating (13) to obtain

$$\chi\Big|_t^{t+\Delta t} = \int_t^{t+\Delta t} R d\tau ,$$

where Δt is the time increment. We now approximate the integral using

$$\int_t^{t+\Delta t} R d\tau \approx \Delta t[\omega R(x, y, t+\Delta t) + (1-\omega)R(x, y, t)] ,$$

where ω is a weight factor. In general, $0 \le \omega \le 1$ and we have used $\omega = 1/2$ which yields the well-known Crank–Nicolson scheme. With this approximation in place we obtain

$$\chi(x, y, t+\Delta t) = \chi(x, y, t) + \Delta t[\omega R(x, y, t+\Delta t) + (1-\omega)R(x, y, t)] . \tag{14}$$

Upon substituting the expression for $R(x, y, t + \Delta t)$ and replacing all spatial derivatives using second-order, central-difference approximations, Eq. (14) becomes a nonlinear system of algebraic equations which is solved using the Gauss–Seidel iterative procedure to determine h and q at time $t + \Delta t$ for all the interior grid points. The convergence criterion adopted is that the maximum difference between successive iterates must be less than a specified tolerance ϵ.

Several numerical experiments were performed in order to determine optimal values for the computational parameters. Unless otherwise stated, the following values were used in all the simulations to be presented and no convergence problems were encountered: $\Delta x = \Delta y = 0.04$, $\Delta t = 0.001$ and $\epsilon = 10^{-7}$. As a numerical check the volume of fluid was computed at each time step and it was found to remain constant to several decimal places. The width of the domain was taken to be $2W = 10$, while the length of the domain depended on the conditions applied along the boundaries. For subcritical flows the limiting unsteady simulations were observed to approach a steady solution, and Neumann conditions were applied along the boundaries. On the other hand, supercritical flows were found to be prone to instabilities which were manifested by the formation of waves along the surface. In this case it made more sense to apply periodic conditions along the upstream and downstream boundaries resulting from a topography that repeated itself in the x direction with the length of the domain corresponding to the distance between successive repetitions. Along the cross-slope boundaries $y = \pm W$ we make use of the symmetry property discussed in the previous section, and thus, apply Neumann conditions. For subcritical flows the values $L_u = -5$ and $L_d = 20$ were used yielding a length of $L_u - L_d = 25$, while for supercritical flows the values $L_u = -10$ and $L_d = 10$ were used. Although most of the topographies considered in this study can be described as smooth localized bumps satisfying the condition that $m(x, y) \to 0$ as $x^2 + y^2 \to \infty$, wavy and trench-like topographies are also explored.

The Neumann conditions were obtained by examining the linearized steady equations at large distances. For subcritical flows we have that $h, q \to 1$ as $x^2 + y^2 \to \infty$. Thus, we set $h = 1 + \hat{h}$ and $q = 1 + \hat{q}$ where $\hat{h}, \hat{q}$ denote small departures from their far-field values, and use them to linearize the steady versions of Eqs. (11)–(12). To leading order this yields

$$\frac{\partial \hat{q}}{\partial x} = 0 , \quad 3\hat{h} - \hat{q} = 0 .$$

Based on this we apply the Neumann conditions given by

$$\frac{\partial h}{\partial x} = \frac{\partial q}{\partial x} = 0 \quad \text{along} \quad x = L_u, L_d ,$$

and similarly

$$\frac{\partial h}{\partial y} = \frac{\partial q}{\partial y} = 0 \text{ along } y = \pm W \ .$$

Lastly, the initial conditions implemented are $h = q = 1$ throughout the entire domain.

4. Results and discussion

The problem is completely characterized by the dimensionless parameters Re, δ, $\cot\beta$, and the topography $\mathcal{M}m(x, y)$. Unless otherwise stated, in all the simulations to be presented the values $\cot\beta = 1$ and $\delta = 0.1$ were used. For a given topography and Reynolds number the criticality of the flow was not known a priori, but rather was determined during the course of the simulations. Once the criticality was established new simulations were performed using the appropriate boundary conditions.

The results are organized as follows. We begin with a subcritical case having $Re = 0.1$ and two symmetrical bottom topographies. Here, we will make comparisons with results obtained using a steady 3D lubrication model (see Appendix A). Following that we will explore a subcritical flow resulting from an asymmetric bottom topography. Then we will discuss some supercritical cases having $Re = 1.5$ together with various one and two-dimensional (2D) bottom topographies. Here, we will make comparisons with an unsteady, second-order 2D IBL model (see Appendix B) for some one-dimensional (1D) topographies. Lastly, we will present some comparisons with experiments for the case of a 2D wavy bottom.

4.1. Subcritical symmetric flow: $Re = 0.1$

For small Reynolds numbers we expect the evolving unsteady flow to eventually approach a steady solution. Indeed, this was observed to be the case for $Re = 0.1$. This small Reynolds number was selected in order to facilitate comparisons with a lubrication model which ignores the inertial terms in the Navier–Stokes equations. The lubrication model was validated by comparing our results with those obtained by Hinton et al. [30]. For the topography given by

$$\mathcal{M} = 0.5 \ , \ m(x, y) = \mathrm{e}^{-(x^2+y^2)} \ ,$$

the maximum and minimum values of the fluid thickness, h_{max} and h_{min}, respectively, were found to be $h_{max} = 1.183$ and $h_{min} = 0.519$ and are in full agreement with those in [30]. The locations of the extrema also appear to agree closely.

Plotted in Fig. 2 are steady contour plots of the fluid thickness using the lubrication and IBL models. Although the contour plots bear a reasonable resemblance, we must keep in mind that the contour values are different in the two plots. Fig. 3 illustrates how quickly the IBL model approaches a steady solution. This diagram shows cross sections of the fluid thickness along the axis of symmetry, $y = 0$, at various times. We see that as time increases the agreement in the profiles persists for larger downstream distances. The profile at $t = 15$ lies on top of that at $t = 10$, and hence, was not included. The corresponding cross sections along the line $x = 0$ quickly approached a steady solution. This is because the flow is mainly in the x direction, with little spanwise flow.

Plotted in Fig. 4 is a comparison in the steady cross sections of the fluid thickness $h(x, y = 0)$ and $h(x = 0, y)$ between the lubrication and IBL models. Here, we notice some significant differences. Although the profiles emerging from the two models have a similar form, the extreme values vary dramatically as do their locations. The lubrication model predicts a much larger difference between the extrema. For example, the lubrication

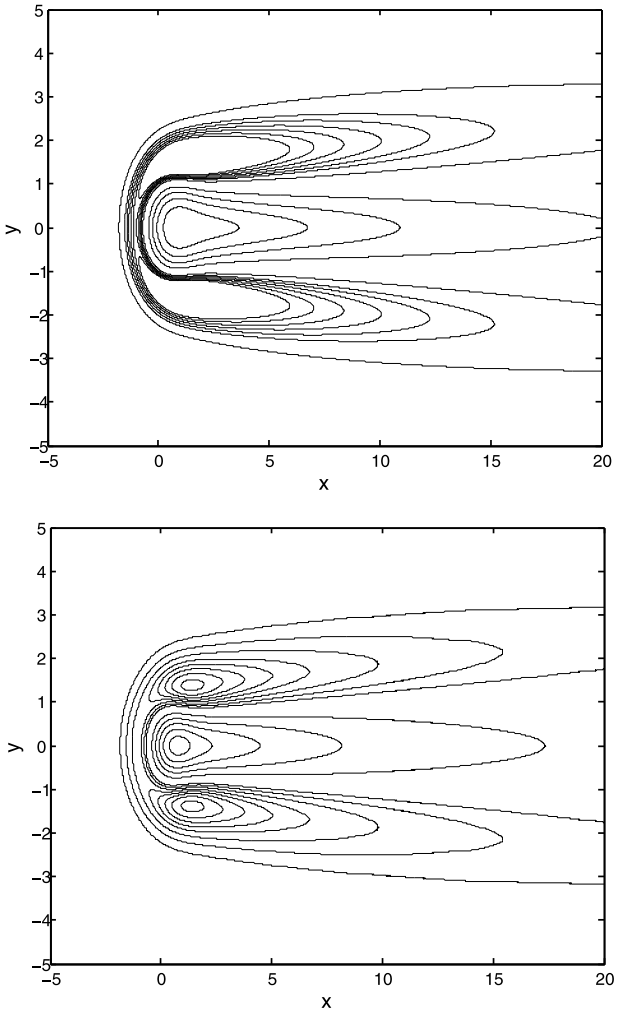

Fig. 2. Top: Contour plot of $h(x, y)$ for $\mathcal{F} = 0.1$ using the steady lubrication model. The contours of h plotted are: 0.6, 0.7, 0.8, 0.9, 1.025, 1.05, 1.06, 1.07, 1.08, 1.09, 1.1. Bottom: Contour plot of $h(x, y, t)$ for $Re = 0.1$ using the unsteady IBL model at $t = 15$. The contours of h plotted are: 0.95, 0.96, 0.97, 0.98, 0.99, 1.0025, 1.005, 1.0075, 1.01, 1.012, 1.014, 1.016, 1.018.

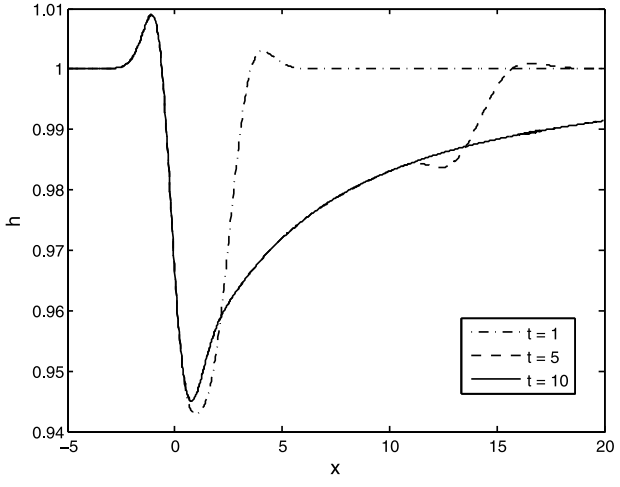

Fig. 3. Cross sections of the fluid thickness $h(x, y = 0, t)$ at times $t = 1, 5, 10$.

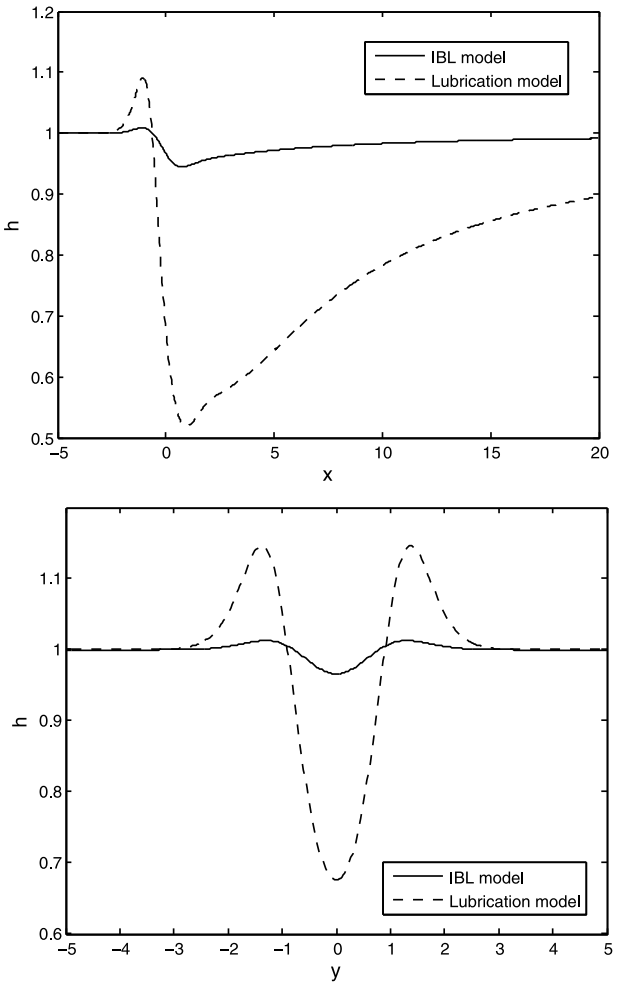

Fig. 4. Top: Comparison in the steady cross sections of the fluid thickness $h(x, y = 0)$. Bottom: Comparison in the steady cross sections of the fluid thickness $h(x = 0, y)$.

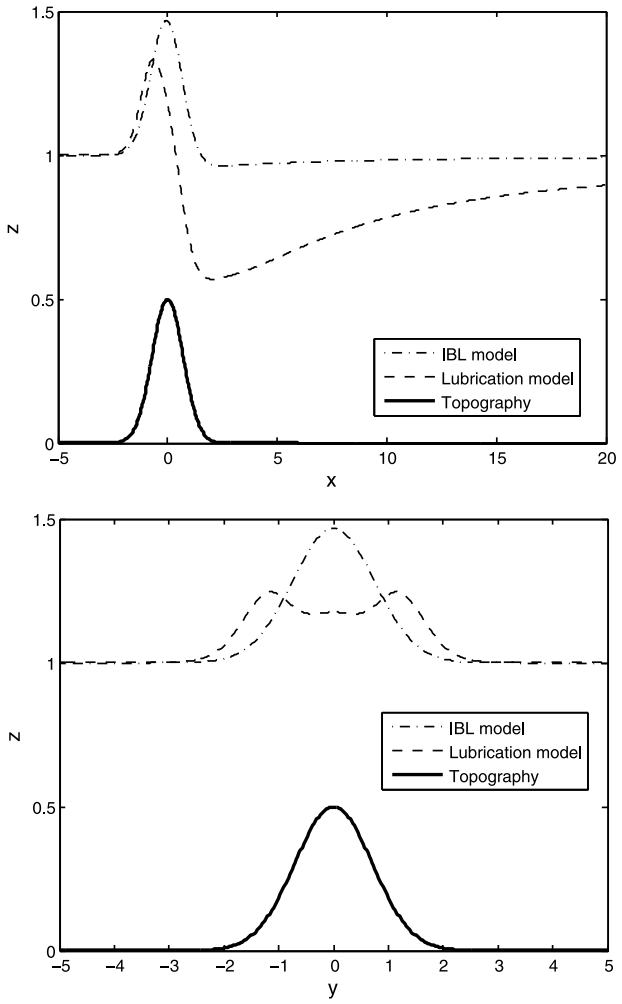

Fig. 5. Top: Comparison in the steady cross sections of the free surface $h(x, y = 0) + \mathcal{M}m(x, y = 0)$. Bottom: Comparison in the steady cross sections of the free surface $h(x = 0, y) + \mathcal{M}m(x = 0, y)$.

model yields $h_{max} = 1.183$ at location $(x, y) = (1.15, \pm 1.55)$ and $h_{min} = 0.519$ at location $(x, y) = (0.95, 0)$, while the IBL model yields the values $h_{max} = 1.019$ and $h_{min} = 0.945$ at locations $(x, y) = (1.375, \pm 1.375)$ and $(x, y) = (0.775, 0)$, respectively. Both models, however, predict that h_{max} and h_{min} occur downstream of the peak in topography. The steady free surface cross sections $h(x, y = 0) + \mathcal{M}m(x, y = 0)$ and $h(x = 0, y) + \mathcal{M}m(x = 0, y)$ are contrasted in Fig. 5. Also included in these diagrams is the bottom topography to provide a sense of the relative positions of the free surface and bottom topography. This clearly shows how close the lubrication model comes to the bottom. Fig. 6 is a close-up contour plot which illustrates the locations of h_{max} and h_{min} for the IBL model. Also shown in the plot is a level curve indicating where the bottom topography reaches one half of the maximum height. We see that h_{min} occurs just inside the backside of the bottom contour, whereas h_{max} occur further downstream and above/below the bottom contour.

A simulation was also conducted using the topography given by

$$\mathcal{M} = 0.5\ ,\ \ m(x, y) = \frac{1}{1 + (x^2 + y^2)^2}\ .$$

Although this topography has the same $\mathcal{M}$ value as the previous case, the height diminishes much more slowly with distance from the origin $(x, y) = (0, 0)$. Despite this, the results obtained were

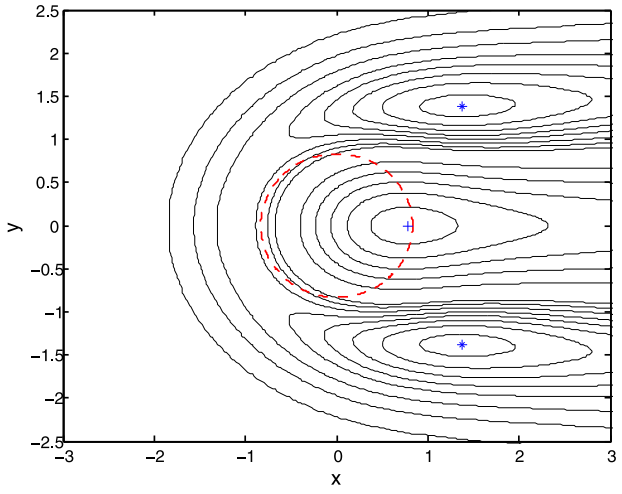

Fig. 6. Close-up contour plot of $h(x, y, t)$ for $Re = 0.1$ using the unsteady IBL model at $t = 15$. The contours plotted are the same as in Fig. 2. The dashed line corresponds to the bottom contour $z = 0.25$. Here, h_{max} is denoted by the symbol $*$, while h_{min} is denoted by the symbol $+$.

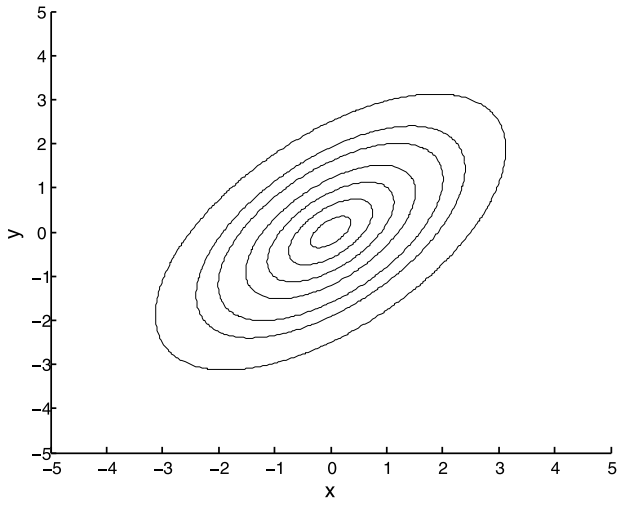

Fig. 7. Level curves for the asymmetric bottom topography. The contours of z plotted are: 0.01, 0.05, 0.1, 0.2, 0.3, 0.4, 0.475.

very similar to the previous case. For example, the lubrication model yields $h_{max} = 1.220$ and $h_{min} = 0.542$, while the IBL model yields the values $h_{max} = 1.023$ and $h_{min} = 0.949$ which are close to the values listed above.

4.2. Subcritical asymmetric flow: $Re = 0.1$

The previous topographies were symmetrical and this resulted in a symmetrical flow. We next consider an asymmetric flow resulting from a topography having

$$\mathcal{M} = 0.5\ ,\ m(x,y) = \mathrm{e}^{-[(\bar{x}/a)^2+(\bar{y}/b)^2]}\ ,$$

where

$$\bar{x} = x\cos\alpha + y\sin\alpha\ ,\ \bar{y} = -x\sin\alpha + y\cos\alpha\ ,$$
$$\alpha = 45^\circ\ ,\ a = 2\ ,\ b = 1\ .$$

As shown in Fig. 7, the level curves corresponding to this topography represent ellipses that are rotated by an angle of $\alpha = 45^\circ$ in the counterclockwise direction about the positive x axis.

For the subcritical case having $Re = 0.1$ the unsteady solution quickly approached a steady solution; beyond $t = 10$ little change was observed in the unsteady solution. Shown in Fig. 8 is a comparison in the steady cross sections of the fluid thickness $h(x, y = 0)$ and $h(x = 0, y)$ between the lubrication and IBL models, while Fig. 9 compares the steady free surface cross sections $h(x, y = 0) + \mathcal{M}m(x, y = 0)$ and $h(x = 0, y) + \mathcal{M}m(x = 0, y)$. The plots reveal similar features as previously noted in Section 4.1. One noteworthy difference is in the asymmetry in the cross section $x = 0$ of the lubrication model, especially when compared to Fig. 5.

Fig. 10 illustrates contour plots of the fluid thickness using the IBL model at times $t = 1$ and $t = 5$, while Fig. 11 contrasts the steady contour plots between the lubrication and IBL models. As time advances we see the contours lengthen in the downstream direction which is to be expected. The contour lines reveal two peaks with a trough in between. Although the contour plots in Fig. 11 portray very similar features, one must bear in mind that the contour values plotted are different in the two plots. There are significant differences in the extreme values of the fluid thicknesses, but the locations of the extrema agree fairly well. For example, the lubrication model yields $h_{max} = 1.231$ at location $(x, y) = (0.1, 1.375)$ and $h_{min} = 0.649$ at location $(x, y) = (1.025, -0.025)$, while the IBL model yields the values $h_{max} = 1.017$ and $h_{min} = 0.962$ at locations $(x, y) = (-0.125, 1.125)$ and $(x, y) = (0.85, -0.075)$, respectively. This highlights the impact of neglecting the inertial terms in the lubrication model, even at the low Reynolds number of $Re = 0.1$ for both symmetrical and asymmetrical flows. Fig. 12 shows a close-up contour plot revealing the locations of h_{max} and h_{min} for the IBL model, as well as a level curve which signals where the bottom topography reaches one half of the maximum height. Here, we see that h_{max} occurs near the upstream side of the bottom contour, whereas h_{min} occurs near the downstream side of the bottom contour which is in agreement with the discovery made by Baxter et al. [29].

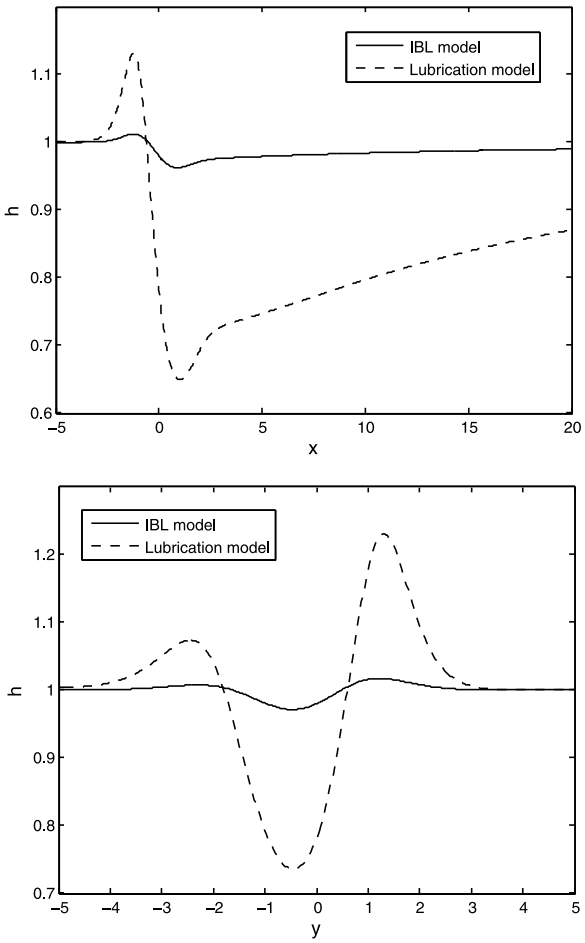

Fig. 8. Top: Comparison in the steady cross sections of the fluid thickness $h(x, y = 0)$. Bottom: Comparison in the steady cross sections of the fluid thickness $h(x = 0, y)$.

4.3. Supercritical flow: $Re = 1.5$

As the Reynolds number increases beyond $Re = 0.1$ the flow eventually becomes unstable. For two-dimensional flow over a flat bottom this occurs when $Re_{crit} = 5\cot\beta/6$ [12–14], and the influence of wavy bottom topography on the stability of the flow has been discussed in previous studies such as [19,42–48]. For example, in [19] using the WRM it is shown that for weak to moderate surface tension bottom topography acts to stabilize the flow, while for stronger surface tension bottom topography can destabilize the flow provided that the wavelengths of the bottom undulations are sufficiently short. The stabilizing effect of bottom topography on inclined flows is also reported in [45] for weak surface tension, whereas the reversal in the stabilizing

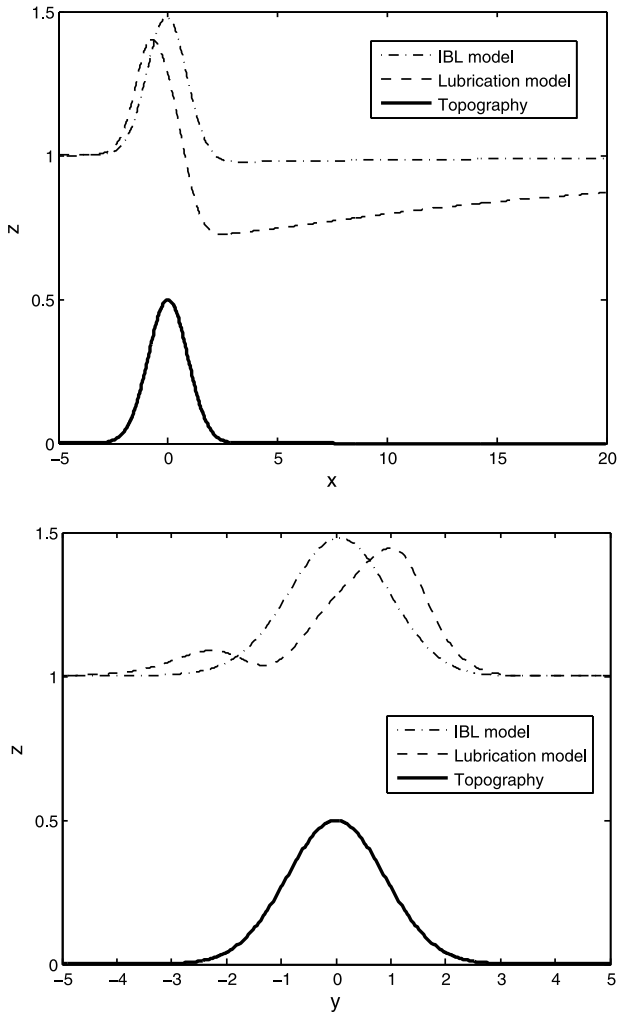

Fig. 9. Top: Comparison in the steady cross sections of the free surface $h(x, y = 0) + \mathcal{M}m(x, y = 0)$. Bottom: Comparison in the steady cross sections of the free surface $h(x = 0, y) + \mathcal{M}m(x = 0, y)$.

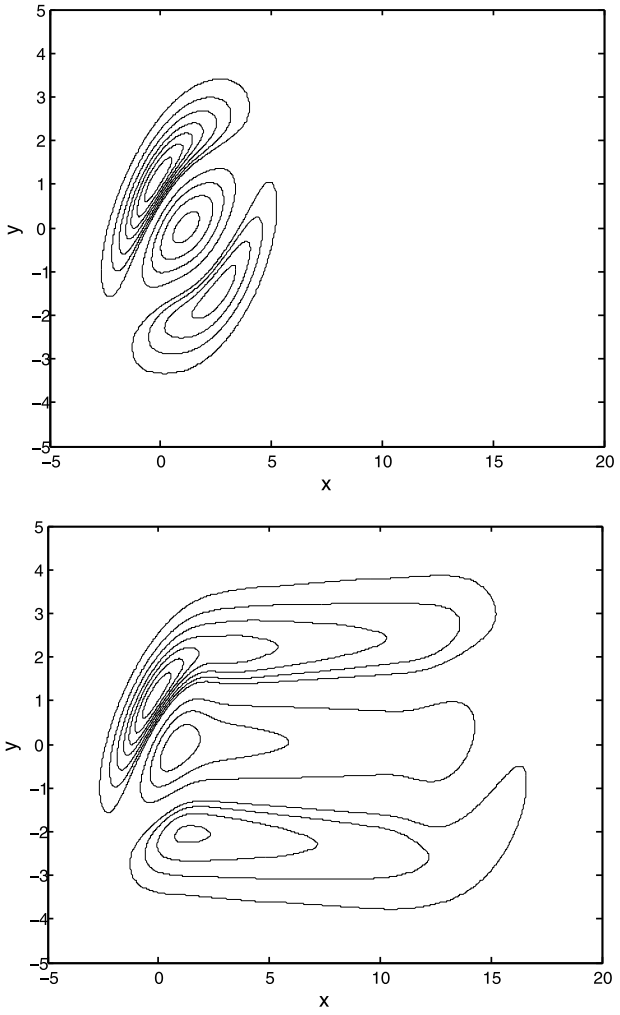

Fig. 10. Contour plots of $h(x, y, t)$ for $Re = 0.1$ using the unsteady IBL model at $t = 1$ (top) and $t = 5$ (bottom). The contours of h plotted are: 0.96, 0.97, 0.98, 0.99, 1.0025, 1.005, 1.0075, 1.01, 1.012, 1.014, 1.016.

action of bottom topography is noted in [42,48] using the WRM. In [42] they investigated the inverse problem, that is, they sought the corresponding bottom topography that gave rise to a free surface profile. On the other hand, [48] addressed the direct problem by expressing the equations of motion in terms of curvilinear coordinates relative to the bottom profile. The work in [43] demonstrated that the critical Reynolds number of the neutral stability curve shifts for gravity-driven films over corrugated bottoms compared to that over flat bottoms. Moreover, the shift depends on several parameters. For large bottom corrugations the study conducted in [44] shows that the fluid particles do not follow the complete solid bottom contour; instead, the particles slide on the separatrix of eddies created in the valleys of the bottom corrugations. In these cases the neutral stability curve changes drastically. For such complex flow structures IBL or WRM methods are not available in the literature.

It is well known that a 2D IBL model overestimates the critical Reynolds number and yields the prediction $Re_{crit} = \cot\beta$ for a flat bottom. For this reason we set $Re = 1.5$ (with $\cot\beta = 1$) to guarantee a supercritical flow for both two and three-dimensional flow. In these simulations periodic boundary conditions were applied along the upstream and downstream boundaries with localized bottom topographies situated at the centre of the domain. As previously noted, applying periodic boundary conditions is equivalent to imposing a periodic topography.

To test the proposed 3D IBL model we ran several simulations using 1D topographies and compared the results with those obtained using the second-order 2D IBL model outlined in Appendix B. The first 1D topography considered is given by

$$\mathcal{M} = 0.5\ ,\ \ m(x) = \mathrm{e}^{-x^2}\ .$$

For small times the output from the two models were indistinguishable. As time progressed small deviations between the two models began to emerge. Fig. 13 contrasts the two models at time $t = 20$. The plots illustrate waves propagating along the free surface which confirms that the flow is unstable. We also notice large peaks appearing in the flow rate q. The differences between the two models, although noticeable, are actually quite small and are the result of differences in the second-order terms in the models. Specifically, the differences can be traced back to the shear condition, $\frac{\partial u}{\partial z}$, applied along the free surface; as outlined in Appendix B, the 2D IBL model utilizes a second-order accurate expression for the shear condition, while the 3D IBL model uses a zero-shear condition. Thus, the impact of using the zero-shear condition instead of a second-order accurate formula is small, and the proposed IBL model behaves like a fully second-order IBL model.

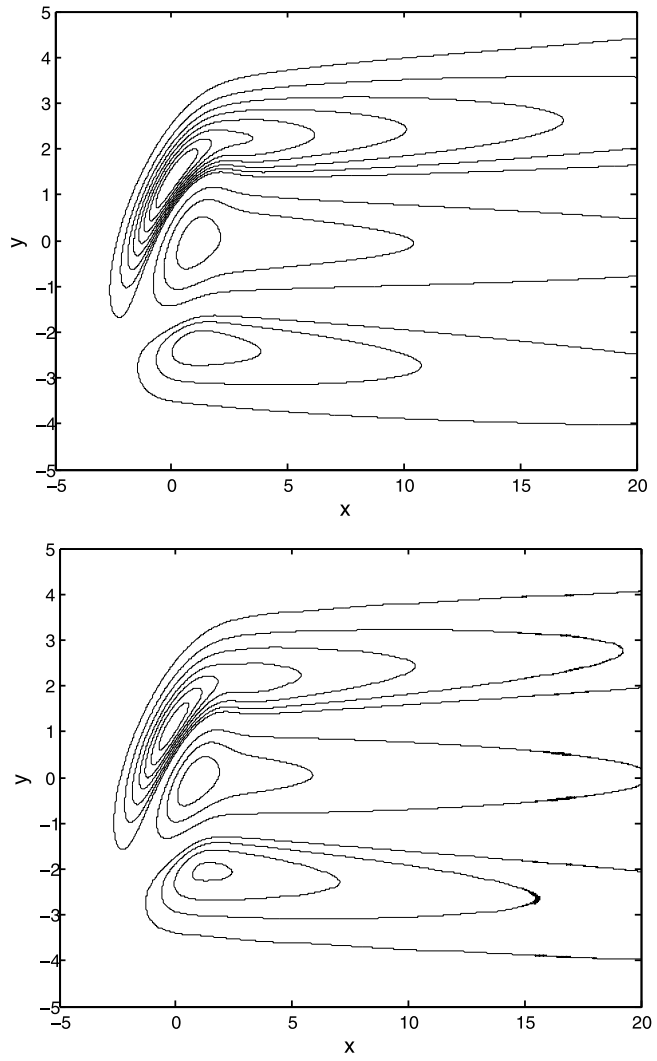

Fig. 11. Top: Contour plot of $h(x, y)$ for $\mathcal{F} = 0.1$ using the steady lubrication model. The contours of h plotted are: 0.7, 0.8, 0.9, 1.025, 1.05, 1.075, 1.1, 1.125, 1.15, 1.175, 1.2. Bottom: Contour plot of $h(x, y, t)$ for $Re = 0.1$ using the unsteady IBL model at $t = 10$. The contours of h plotted are: 0.96, 0.97, 0.98, 0.99, 1.0025, 1.005, 1.0075, 1.01, 1.012, 1.014, 1.016.

The second 1D topography considered corresponds to a wavy bottom having

$$\mathcal{M} = 0.5\ ,\ \ m(x) = \cos(2\pi x)\ .$$

As in the previous case, the output from the two models were very similar. For example, Fig. 14 illustrates the free surface predicted by the two models at $t = 20$. We see that the free surface from both models are close to one another and are in phase with the bottom topography.

The last 1D topography considered is a steep-sided trench. Previous studies [28,36,37] have approximated a trench using the arctangent function given by

$$\mathcal{M}m(x) = \frac{\mathcal{M}}{2\tan^{-1}\left(\frac{l}{2\lambda}\right)}\left[\tan^{-1}\left(\frac{x+\frac{l}{2}}{\lambda}\right) - \tan^{-1}\left(\frac{x-\frac{l}{2}}{\lambda}\right)\right]\ .$$

Here, l and $\mathcal{M} < 0$, denote the length and depth of the trench, respectively, while λ is a steepness parameter. Shown in Fig. 15 is a simulation with trench parameters $l = 2$, $\mathcal{M} = -0.5$ and $\lambda = 0.005$ at time $t = 5$ using the 3D IBL model (the 2D IBL model is not shown since the result was indistinguishable from the 3D IBL model). We see that the free surface closely mirrors the topography except at the edges where it overshoots.

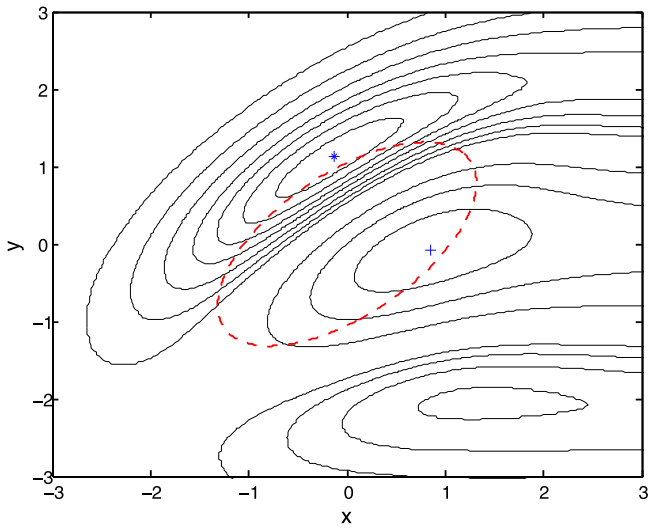

Fig. 12. Close-up contour plot of $h(x, y, t)$ for $Re = 0.1$ using the unsteady IBL model at $t = 10$. The contours plotted are the same as in Fig. 11. The dashed line corresponds to the bottom contour $z = 0.25$. Here, h_{max} is denoted by the symbol $*$, while h_{min} is denoted by the symbol $+$.

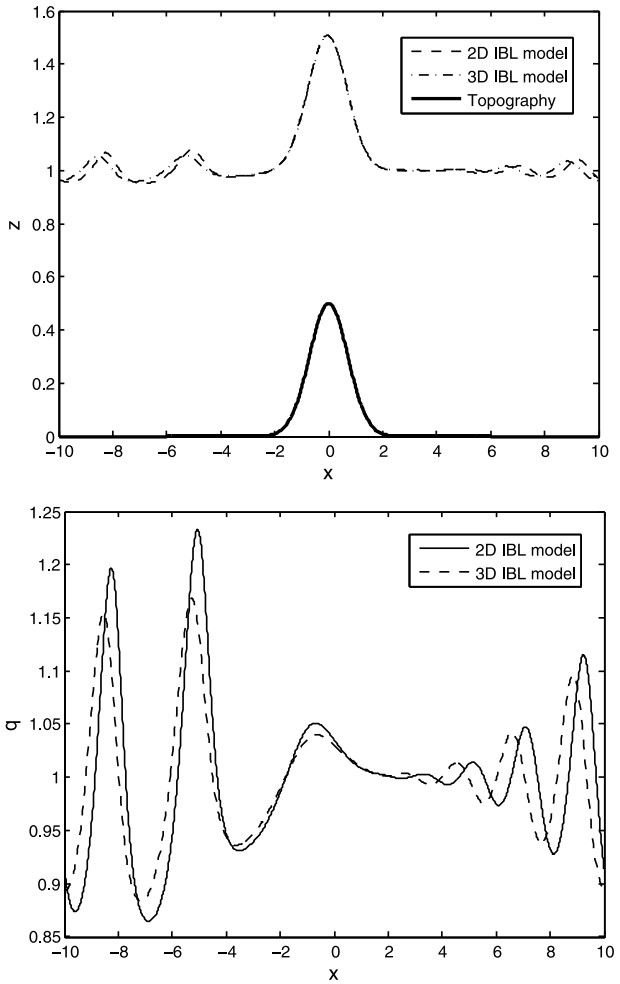

Fig. 13. Comparison in the free surface $h + \mathcal{M}m$ (top) and q (bottom) between the 2D and 3D IBL models for $Re = 1.5$ at time $t = 20$.

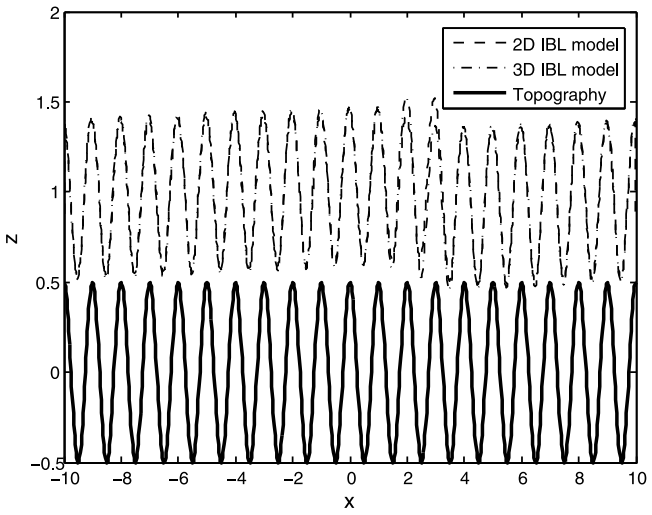

Fig. 14. Comparison in the free surface $h + \mathcal{M}m$ between the 2D and 3D IBL models for $Re = 1.5$ at time $t = 20$.

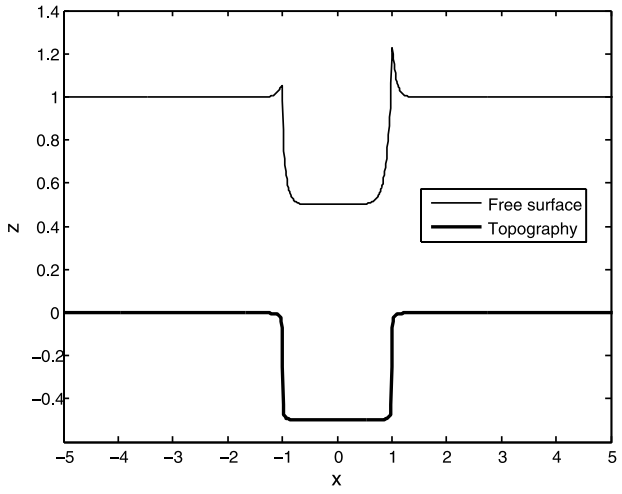

Fig. 15. The free surface $h+\mathcal{M}m$ for flow over a trench using the 3D IBL model for $Re = 1.5$, $\delta = 0.1$ and $\cot\beta = 1$ at time $t = 5$.

We next present a simulation having the 2D topography prescribed by

$$\mathcal{M} = 0.5\ ,\ \ m(x, y) = \mathrm{e}^{-(x^2+y^2)}\ .$$

Plotted in Fig. 16 are contour plots of the fluid thickness using the 3D IBL model at times $t = 10$ and $t = 20$. The plots clearly demonstrate the unsteadiness of the flow, and how the patterns become more complex with time. The contours portray a series of peaks and troughs in fluid thickness which evolve in time, and resemble those of vortex shedding from a circular cylinder. The difference is that instead of having eddies of recirculating flow, here we have eddies of fluid thickness. The topography has a ripple effect in the downstream flow causing waves to form on the free surface. At $t = 20$ we see a series of waves approaching the topography from the left as a result of the periodicity conditions. Lastly, shown in Fig. 17 are cross sections of the free surface and flow rate along the plane of symmetry $y = 0$. Also shown in these diagrams are the results obtained using the 2D IBL model to illustrate the three-dimensional nature of the flow. We notice that the profiles for the free surface and flow rate from the two models have similar forms. An apparent difference is that the profile arising from the 3D model is shifted

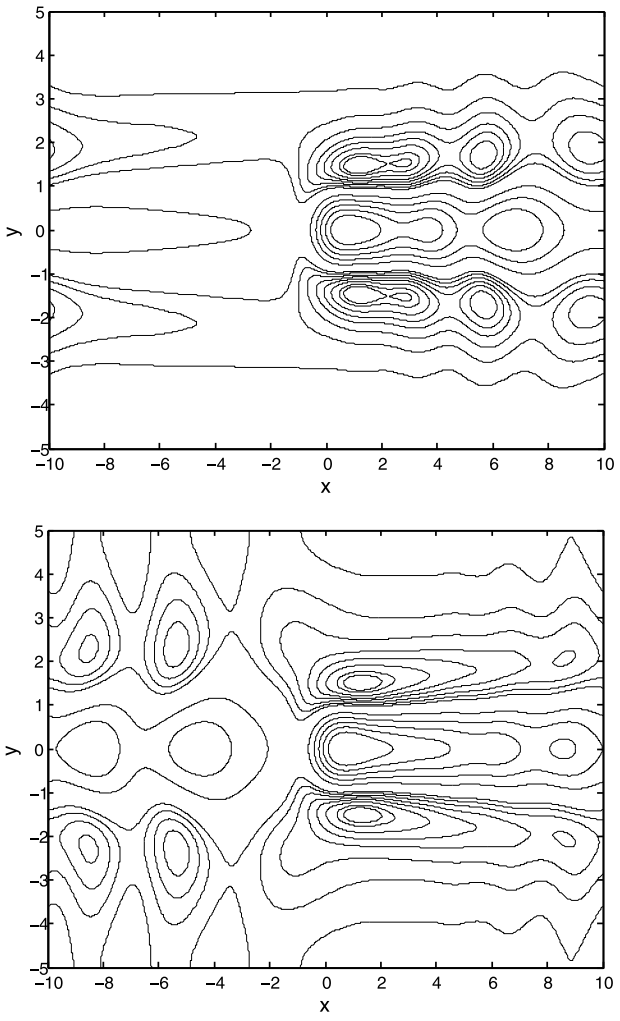

Fig. 16. Contour plots of $h(x, y, t)$ for $Re = 1.5$ using the 3D IBL model at $t = 10$ (top) and $t = 20$ (bottom). The contours of h plotted are: 0.95, 0.96, 0.97, 0.98, 0.99, 1.0025, 1.005, 1.0075, 1.01, 1.012, 1.014, 1.016, 1.017.

vertically downward from that obtained using the 2D model. This is especially noticeable in the profile for q. This is due to the spanwise flow which is responsible for diverting fluid from the plane of symmetry in response to the bottom topography. Thus, although the spanwise flow is small it does have an effect on the flow causing some departures from two-dimensional flow. To emphasize this we compare Figs. 13 and 17. In Fig. 13 both models used the 1D topography $m(x) = \mathrm{e}^{-x^2}$ which yielded good agreement in the results at $t = 20$. On the other hand, in Fig. 17 the 2D IBL model used the topography $m(x) = \mathrm{e}^{-x^2}$, while the 3D IBL model used the topography $m(x, y) = \mathrm{e}^{-(x^2+y^2)}$, and this resulted in noticeable differences in the profiles at the smaller time $t = 10$.

4.4. Comparisons with experiments

We conclude this section by discussing some comparisons with experiments. For this purpose we have used the experimental results from Heining et al. [40]. In their investigation they considered steady gravity-driven free surface 3D flows over periodic corrugations having

$$\mathcal{M}m(x) = \mathcal{M}[\cos x + \cos y]\ ,$$

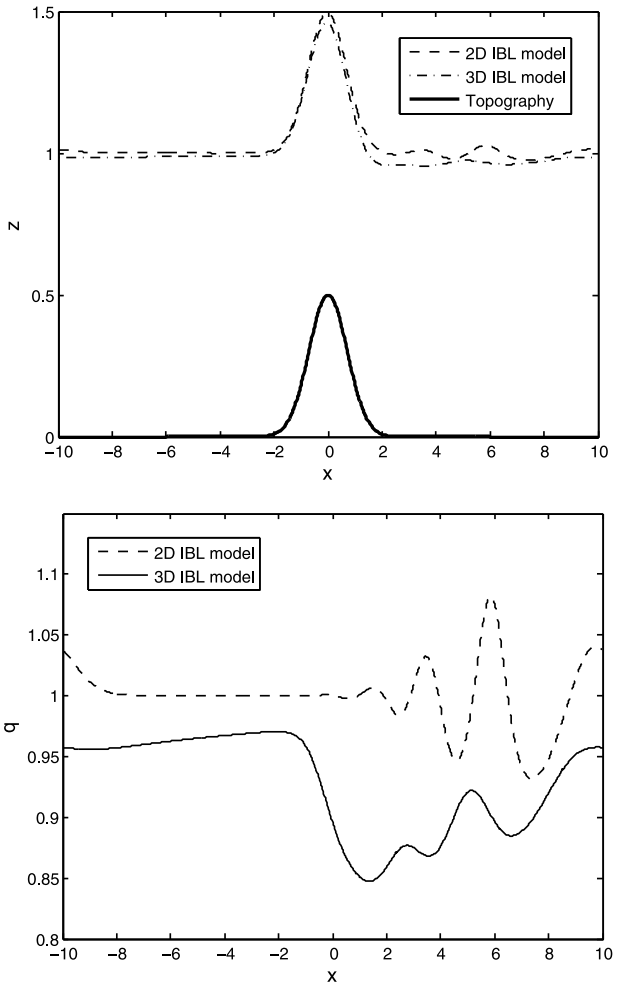

Fig. 17. Comparison in the free surface $h + \mathcal{M}m$ (top) and q (bottom) between the 2D and 3D IBL models for $Re = 1.5$ at time $t = 10$.

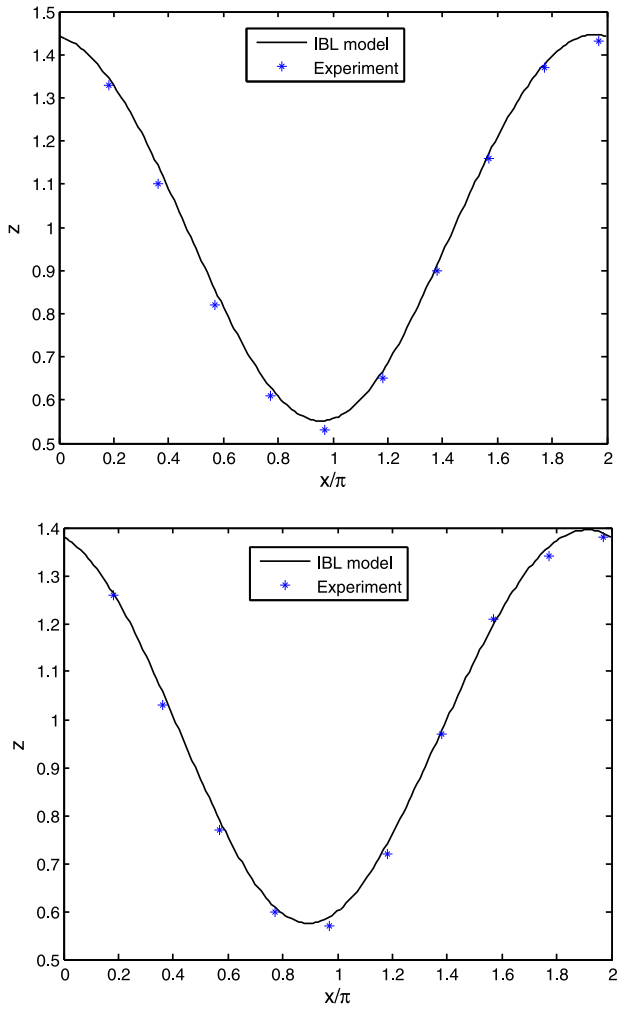

Fig. 18. Comparison in the cross section of the free surface $h + \mathcal{M}m$ along $y = 0$ (top) and $y = \pi$ (bottom) between the 3D IBL model and experimental data taken from [40].

and tackled the problem analytically, numerically and experimentally. The analytical work followed an integral-boundary-layer approach, and took the form of an expansion in powers of the steepness parameter which is valid for small $\mathcal{M}$. The numerical work, on the other hand, made use of the open source CFD software OpenFOAM. The liquids used in the experiments were silicone oils; the free surface was tracked mechanically using a needle and highspeed camera while the free surface flow was visualized using carbon powder tracer particles. They considered both weakly and strongly corrugated topographies.

For our comparisons we will focus on the weakly corrugated case where the bottom topography is fully submerged. The parameters used in our simulations matched those in the experiment and are given by

$$Re = 0.0143\ ,\ \beta = 11^\circ\ ,\ \delta = \sqrt{0.019}\ ,\ \mathcal{M} = 0.442\ .$$

Computations using the proposed 3D IBL model were carried out over the rectangular domain $0 \le x \le 2\pi$, $0 \le y \le \pi$ using periodic conditions at $x = 0$ and $x = 2\pi$, and Neumann conditions at $y = 0$ and $y = \pi$ with a uniform grid spacing of $\pi/100$ in both the x and y directions. Simulations were run to $t = 15$ to ensure that a steady solution was attained. Shown in Fig. 18 are cross sections of the free surface along $y = 0$ and $y = \pi$, contrasting numerical and experimental results. We see good agreement between the IBL model predictions and the experiments which is comparable to the agreement between the numerics and analytics in [40]. Thus, this indirectly shows that the IBL model agrees well with their analytical work as well as the results obtained using the OpenFOAM software.

5. Conclusions

Presented in this paper is the three-dimensional steady and unsteady gravity-driven flow down an incline and over one and two-dimensional topographies. A new three-dimensional IBL model was constructed for flows which are primarily unidirectional by blending lubrication theory and IBL modelling. A numerical investigation using Neumann and periodic far-field boundary conditions was then conducted based on the derived model where comparisons were made with a steady three-dimensional lubrication model, an unsteady two-dimensional IBL model, and with experiments. Various bottom topographies were considered including smooth localized bumps, periodic corrugations, and a steep-sided trench.

Although the lubrication model predictions have similar profiles as those of the new model, noticeable differences in extreme values were observed which highlights a shortcoming of lubrication theory. In spite of the fact that the flow was mainly two dimensional, some departures were observed when contrasted with the results obtained using an unsteady, two-dimensional, second-order, IBL model. This shows that the spanwise flow, despite

being small, has an impact on the overall flow. For low Reynolds numbers the unsteady flow approached a steady solution for all the symmetrical and asymmetrical topographies considered; however, for larger Reynolds numbers the flow became unstable and succumbed to the formation of waves along the surface. Lastly, good agreement between the proposed IBL model and experiments was found for the case of a two-dimensional weakly wavy bottom.

Declaration of competing interest

The authors declare that they have no known competing financial interests or personal relationships that could have appeared to influence the work reported in this paper.

Data availability

Data will be made available on request

Acknowledgement

This research did not receive any specific grant from funding agencies in the public, commercial, or not-for-profit sectors.

Appendix A. Three-dimensional lubrication model

The steady lubrication model employed in this investigation is identical to that derived by Hinton et al. [30]. Here, we will only highlight the departures from their model as per the recent work by D'Alessio [33]. We begin by stating the governing equation in dimensionless form developed in [30] for the fluid thickness, $h(x,y)$, above the bottom topography denoted by $\mathcal{M}m(x,y)$ where $\mathcal{M}$ is a dimensionless parameter

$$\frac{\partial}{\partial x}(h^3) = \mathcal{F}\left[\frac{\partial}{\partial x}\left(h^3\frac{\partial h}{\partial x}\right)+\frac{\partial}{\partial y}\left(h^3\frac{\partial h}{\partial y}\right)\right]+\mathcal{M}\left[\frac{\partial}{\partial x}\left(h^3\frac{\partial m}{\partial x}\right)+\frac{\partial}{\partial y}\left(h^3\frac{\partial m}{\partial y}\right)\right]. \tag{A.1}$$

In the above, the dimensionless parameter $\mathcal{F}=\delta\cot\beta$. As pointed out in the alternate formulation proposed in [33], for numerical purposes it makes sense to introduce the flow variable $\eta = h^4$. Eq. (A.1) then takes the final form

$$3\frac{\partial\eta}{\partial x} = \mathcal{F}\eta^{1/4}\left(\frac{\partial^2\eta}{\partial x^2}+\frac{\partial^2\eta}{\partial y^2}\right)+4\mathcal{M}\eta\left(\frac{\partial^2 m}{\partial x^2}+\frac{\partial^2 m}{\partial y^2}\right)+3\mathcal{M}\left(\frac{\partial m}{\partial x}\frac{\partial\eta}{\partial x}+\frac{\partial m}{\partial y}\frac{\partial\eta}{\partial y}\right), \tag{A.2}$$

or more conveniently as

$$\frac{\partial^2\eta}{\partial x^2}+\frac{\partial^2\eta}{\partial y^2}+A\frac{\partial\eta}{\partial x}+B\frac{\partial\eta}{\partial y}+C\eta = 0, \tag{A.3}$$

where

$$A=\frac{3}{\mathcal{F}\eta^{1/4}}\left(\mathcal{M}\frac{\partial m}{\partial x}-1\right),\quad B=\frac{3\mathcal{M}}{\mathcal{F}\eta^{1/4}}\frac{\partial m}{\partial y},$$
$$C=\frac{4\mathcal{M}}{\mathcal{F}\eta^{1/4}}\left(\frac{\partial^2 m}{\partial x^2}+\frac{\partial^2 m}{\partial y^2}\right).$$

Equation (A.3) was solved using finite differences [41]. We note that although A, B and C depend on η, in the iterative solution procedure soon to be described we can use the previous iterate of η, and hence, view it as known, albeit approximately. Replacing all derivatives by second-order, central-difference approximations results in the following nonlinear algebraic system of equations

$$\begin{aligned}&(1+\frac{1}{2}A_{i,j}\Delta x)\eta_{i+1,j}+(1-\frac{1}{2}A_{i,j}\Delta x)\eta_{i-1,j}\\&+\frac{(\Delta x)^2}{(\Delta y)^2}\left(1+\frac{1}{2}B_{i,j}\Delta y\right)\eta_{i,j+1}\\&+\frac{(\Delta x)^2}{(\Delta y)^2}\left(1-\frac{1}{2}B_{i,j}\Delta y\right)\eta_{i,j-1}\\&=\left[2+2\left(\frac{\Delta x}{\Delta y}\right)^2-C_{i,j}(\Delta x)^2\right]\eta_{i,j},\end{aligned}$$

where the notation $\eta_{i,j}=\eta(x_i,y_j)$ was adopted and $\Delta x, \Delta y$ denote the uniform grid spacings in the x, y directions, respectively. The above system of equations was solved using a Gauss–Seidel iterative procedure for all interior grid points (x_i, y_j). Along the boundaries of the computational domain an asymptotic gradient condition derived in [33] was implemented. As an initial guess $\eta_{i,j}=1$ was used throughout the entire computational domain and along the boundaries. The convergence criterion adopted was that the maximum difference between successive iterates must be less than a specified tolerance ϵ. Once convergence is reached we then switch back to the original variable using $h=\eta^{1/4}$. No convergence problems were encountered.

Appendix B. Two-dimensional IBL model

Here we briefly explain how an unsteady, two-dimensional, second-order IBL model can be derived. We begin by listing the continuity and horizontal momentum equations in dimensionless form to second order

$$\frac{\partial u}{\partial x}+\frac{\partial w}{\partial z}=0, \tag{B.1}$$

$$\delta Re\left(\frac{\partial u}{\partial t}+u\frac{\partial u}{\partial x}+w\frac{\partial u}{\partial z}\right)=-\delta Re\frac{\partial p}{\partial x}+3+\delta^2\frac{\partial^2 u}{\partial x^2}+\frac{\partial^2 u}{\partial z^2}. \tag{B.2}$$

The pressure can be eliminated by solving the first-order approximation to the vertical momentum equation given by

$$Re\frac{\partial p}{\partial z}=-3\cot\beta+\delta\frac{\partial^2 w}{\partial z^2},$$

subject to

$$p=\frac{2\delta}{Re}\frac{\partial w}{\partial z}\quad\text{at}\quad z=\zeta+h,$$

where $\zeta(x)$ denotes the one-dimensional bottom topography. We then integrate Eq. (B.2) from $z=\zeta$ to $z=\zeta+h$ and make use of the following stress and kinematic conditions along the surface $z=\zeta+h$

$$\frac{\partial u}{\partial z}=4\delta^2\left(\zeta'+\frac{\partial h}{\partial x}\right)\frac{\partial u}{\partial x}-\delta^2\frac{\partial w}{\partial x},$$
$$w=\frac{\partial h}{\partial t}+u\left(\zeta'+\frac{\partial h}{\partial x}\right),$$

and the no-slip conditions $u=w=0$ along the bottom $z=\zeta$. In the above the prime refers to differentiation with respect to x.

Following a similar procedure as that outlined in Section 2 using the profile

$$u=\frac{3q}{2h^3}(z-\zeta)(2h-z+\zeta)\quad\text{where}\quad q=\int_\zeta^{\zeta+h}u\,dz,$$

then leads to the following second-order IBL equations

$$\frac{\partial h}{\partial t}+\frac{\partial q}{\partial x}=0, \tag{B.3}$$

$$\frac{\partial q}{\partial t}+\frac{\partial}{\partial x}\left(\frac{6}{5}\frac{q^2}{h}+\frac{3\cot\beta}{2Re}h^2\right)=\frac{3}{\delta Re}\left(h-\frac{q}{h^2}\right)-\frac{3\cot\beta}{Re}h\zeta'$$

$$+\frac{\delta}{Re}\left[\frac{9}{2}\frac{\partial^2 q}{\partial x^2}-\frac{6q}{h}\frac{\partial^2 h}{\partial x^2}\right.$$
$$-\frac{9q\zeta''}{2h}+\frac{3q\zeta'}{h^2}\frac{\partial h}{\partial x}-\frac{3\zeta'}{h}\frac{\partial q}{\partial x}-\frac{6}{h}\frac{\partial h}{\partial x}\frac{\partial q}{\partial x}+\frac{6q}{h^2}\left(\frac{\partial h}{\partial x}\right)^2$$
$$\left.-\frac{6q(\zeta')^2}{h^2}\right]. \tag{B.4}$$

System (B.3)–(B.4) was solved using the fractional-step method and the details can be found in [19].

References

[1] S. Kalliadasis, C. Ruyer-Quil, B. Scheid, M.G. Velarde, Falling Liquid Films, Springer-Verlag, London, 2012.
[2] R.V. Craster, O.K. Matar, Dynamics and stability of thin liquid films, Rev. Modern Phys. 81 (2009) 1131–1198.
[3] H.C. Chang, Wave evolution on a falling film, Annu. Rev. Fluid Mech. 26 (1994) 103–136.
[4] S.F. Kistler, P.M. Schweizer, Liquid Film Coating: Scientific Principles and their Technological Implications, Chapman and Hall, London, 1997.
[5] R.W. Griffiths, The dynamics of lava flows, Annu. Rev. Fluid Mech. 32 (2000) 477–518.
[6] H.E. Huppert, J.B. Shepherd, R.H. Sigurdsson, R.S.J. Sparks, On lava dome growth, with applicationto the 1979 lava extrusion of the Soufriere of St. Vincent, J. Volc. Geotherm. Res. 14 (1982) 199–222.
[7] E. Rignot, J. Mouginot, B. Scheuchl, Ice flow of the antarctic ice sheet, Science 333 (6048) (2011) 1427–1430.
[8] C.O. Ng, C.C. Mei, Roll waves on a shallow layer of mud modelled as a power-law fluid, J. Fluid Mech. 263 (1994) 151–183.
[9] K.M. Hákonardóttir, A.J. Hogg, J. Batey, A.W. Woods, Flying avalanches, Geophys. Res. Lett. 30 (2003) 2191.
[10] R.J. Braun, Dynamics of the tear film, Annu. Rev. Fluid Mech. 44 (2012) 267–297.
[11] P.L. Kapitza, S.P.S.P. Kapitza, Wave flow of thin layers of a viscous fluid: III. Experimental study of undulatory flow conditions, J. Exp. Theor. Phys. 19 (1949) 105–120.
[12] T.B. Benjamin, Wave formation in laminar flow down an inclined plane, J. Fluid Mech. 2 (1957) 554–574.
[13] C.-S. Yih, Stability of liquid flow down an inclined plane, Phys. Fluids 6 (1963) 321–334.
[14] D.J. Benney, Long waves on liquid films, J. Math. Phys. 45 (1966) 150–155.
[15] V.Y. Shkadov, Wave conditions in flow of thin layer of a viscous liquid under the action of gravity, Izv. Akad. Nauk SSSR Mekh. Zhidk. Gaza 1 (1) (1967) 43–51.
[16] C. Ruyer-Quil, P. Manneville, Improved modeling of flows down inclined planes, Eur. Phys. J. B 15 (2000) 357–369.
[17] C. Ruyer-Quil, P. Manneville, Further accuracy and convergence results on the modelingof flows down inclined planes by weighted-residual approximations, Phys. Fluids 14 (2002) 170–183.
[18] S. Kalliadasis, E.A. Demekhin, C. Ruyer-Quil, M.G. Velarde, Thermocapillaryinstability and wave formation on a film falling down a uniformly heated plane, J. Fluid Mech. 492 (2003) 303–338.
[19] S.J.D. D'Alessio, J.P. Pascal, H.A. Jasmine, Instability in gravity-driven flow over uneven surfaces, Phys. Fluids 21 (2009) 062105.
[20] J.P. Pascal, S.J.D. D'Alessio, Instability in gravity-driven flowover uneven permeable surfaces, Int. J. Multiph. Flow. 36 (2010) 449–459.
[21] S.J.D. D'Alessio, J.P. Pascal, E. Ellaban, C. Ruyer-Quil, Marangoni instabilities associated with heated surfactant-laden falling films, J. Fluid Mech. 887 (2020) A20.
[22] S.J.D. D'Alessio, J.P. Pascal, H.A. Jasmine, K.A. Ogden, Film flow over heated wavy inclined surfaces, J. Fluid Mech. 665 (2010) 418–456.
[23] G.R. Daly, P.H. Gaskell, S. Veremieiev, Gravity-driven film flow down a uniformly heated, smoothly corrugated rigid substrate, J. Fluid Mech. 930 (2022) A23.
[24] S. Veremieiev, D.H. Wacks, Modelling gravity-driven film flow on inclined corrugatedsubstrate using a high fidelity weighted residual integral boundary-layer method, Phys. Fluids 31 (2019) 022101.
[25] S. Kalliadasis, C. Bielarz, G. Homsy, Steady free-surface thin film flows over topography, Phys. Fluids 12 (2000) 1889–1898.
[26] C. Bielarz, S. Kalliadasis, Time-dependent free-surface thin film flows over topography, Phys. Fluids 15 (2003) 2512–2524.
[27] A. Mazouchi, G.M. Homsy, Free surface Stokes flow over topography, Phys. Fluids 13 (2001) (2001) 2751–2761.
[28] P.H. Gaskell, P.K. Jimack, M. Sellier, H.M. Thompson, M.C.T. Wilson, Gravity-driven flow of continuous thin liquid films on non-porous substrates with topography, J. Fluid Mech. 509 (2004) 253–280.
[29] S.J. Baxter, H. Power, K.A. Cliffe, S. Hibberd, Three-dimensional thin film flow over andaround an obstacle on an inclined plane, Phys. Fluids 21 (2009) 032102.
[30] E.M. Hinton, A.J. Hogg, H.E. Huppert, Interaction of viscous free-surface flows with topography, J. Fluid Mech. 876 (2019) 912–938.
[31] E.M. Hinton, A.J. Hogg, H.E. Huppert, Shallow free-surface Stokes flow around a corner, Phil. Trans. R. Soc. A 378 (2020) 20190515.
[32] E.M. Hinton, A.J. Hogg, H.E. Huppert, Viscous free-surface flows past cylinders, Phys. Rev. Fluids 5 (2020) 084101.
[33] S.J.D. D'Alessio, Obstructed gravity-driven flow down an incline, Acta Mech. 234 (2023) 3575–3594.
[34] N. Aksel, M. Schörner, Films over topography: from creeping flow to linear stability, theory, and experiments, a review, Acta Mech. 229 (2018) 1453–1482.
[35] N.R. Buttle, R. Pethiyagoda, T.J. Moroney, S.W. McCue, Three-dimensional free-surface flow overarbitrary bottom topography, J. Fluid Mech. 846 (2018) 166–189.
[36] S. Veremieiev, H.M. Thompson, Y.C. Lee, P.H. Gaskell, Inertial thin film flow on planar surfaces featuring topography, Comput. & Fluids 39 (2010) 431–450.
[37] S. Veremieiev, H.M. Thompson, P.H. Gaskell, Free-surface film flow over topography: Full three-dimensional finite element solutions, Comput. & Fluids 122 (2015) 66–82.
[38] M.M.J. Decré, J.C. Baret, Gravity-driven flows of low-viscosity liquids over two-dimensional topographies, J. Fluid Mech. 487 (2003) 147–166.
[39] Y.Y. Trifonov, Viscous film flow down corrugated surfaces, J. Appl. Mech. Tech. Phys. 45 (2004) 389–400.
[40] C. Heining, T. Pollak, N. Aksel, Pattern formation and mixing in three-dimensional film flow, Phys. Fluids 24 (2012) 042102.
[41] R.J. LeVeque, Finite Difference Methods for Ordinary and Partial Differential Equations - Steady-State and Time-Dependent Problems, SIAM, Philadelphia, 2007.
[42] C. Heining, N. Aksel, Bottom reconstruction in thin-film flow over topography: steadysolution and linear stability, Phys. Fluids 21 (2009) 083605.
[43] C. Heining, N. Aksel, Effects of inertia and surface tension on a power-law fluid flowing down a wavy incline, Int. J. Multiph. Flow. 36 (2010) 847–857.
[44] A. Wierschem, N. Aksel, Instability of a liquid film flowing down an inclined wavy plane, Physica D 186 (2003) 221–237.
[45] A. Wierschem, C. Lepski, N. Aksel, Effect of long undulated bottoms on thin gravity-driven films, Acta Mech. 179 (2005) 41–66.
[46] T. Pollak, N. Aksel, Crucial flow stabilization and multiple instability branches of gravity-driven films over topography, Phys. Fluids 25 (2013) 024103.
[47] Y.Y. Trifonov, Stability and nonlinear wavy regimes in downward film flows on a corrugated surface, J. Appl. Mech. Tech. Phys. 48 (2007) 91–100.
[48] T. Häcker, H. Uecker, An integral boundary layer equation for film flow over inclined wavy bottoms, Phys. Fluids 21 (2009) 092105.